Regulation of Photovoltaic Voltage

Weidong Xiao, *Student Member, IEEE*, William G. Dunford, *Senior Member, IEEE*, Patrick R. Palmer, *Member, IEEE*, and Antoine Capel

***Abstract*—In photovoltaic power systems, both photovoltaic modules and switching-mode converters present nonlinear and time-variant characteristics, which result in a difficult control problem. This paper presents an in-depth analysis and modeling to discover the inherent features of a photovoltaic power system. The method of successive linearization simplifies the nonlinear problem back to the linear case. This paper also presents the use of Youla parameterization to design a stable control system for regulating the photovoltaic voltage. The experimental and simulation results demonstrate the effectiveness of the presented analysis, design, and implementation.**

***Index Terms*—Digital control, modeling, Nyquist stability, photovoltaic power systems, voltage control.**

I. Introduction

COMPARED to space application, significant solar radiation is filtered and blocked by the atmosphere and cloud cover before it is received at the earth surface. Atmospheric variables dramatically affect the available insolation for photovoltaic generators. Consequently, the current–voltage (I–V) curves and maximum power points (MPPs) of photovoltaic modules change with the solar radiation, as illustrated in Fig. 1, where G_a symbolizes the solar insolation. Besides insolation, another important factor that influences the characteristics of a photovoltaic module is cell temperature, as shown in Fig. 2. The variation of cell temperature changes the MPP greatly along the x-axis. Fig. 3 illustrates the temperature effect based on the relationship of photovoltaic power and current. These specifications of BP350 are obtained from the product datasheet, which is tabulated in the Appendix.

As shown in Figs. 1–3, both the photovoltaic voltage and the photovoltaic current at the MPP can represent the MPP. For a particular operating condition, the control of MPP tracking normally regulates either the voltage or current to a certain value that represents the local MPP. However, these conditions are time variant with the change of insolation and temperature.

Manuscript received October 10, 2006; revised January 10, 2007. Abstract published on the Internet January 27, 2007.

W. Xiao is with the University of British Columbia, Vancouver, BC V6T 1Z4, Canada (e-mail: weidongx@ece.ubc.ca).

W. G. Dunford is with the Department of Electrical and Computer Engineering, University of British Columbia, Vancouver, BC V6T 1Z4, Canada.

P. R. Palmer is with St. Catharine's College, University of Cambridge, Cambridge CB2 1Rl, U.K., and also with the Department of Electrical and Computer Engineering, University of British Columbia, Vancouver, BC V6T 1Z4, Canada.

A. Capel is with the School of Engineering, Universitat Rovira i Virgili, 43005 Tarragona, Spain.

Color versions of one or more of the figures in this paper are available online at http://ieeexplore.ieee.org.

Digital Object Identifier 10.1109/TIE.2007.893059

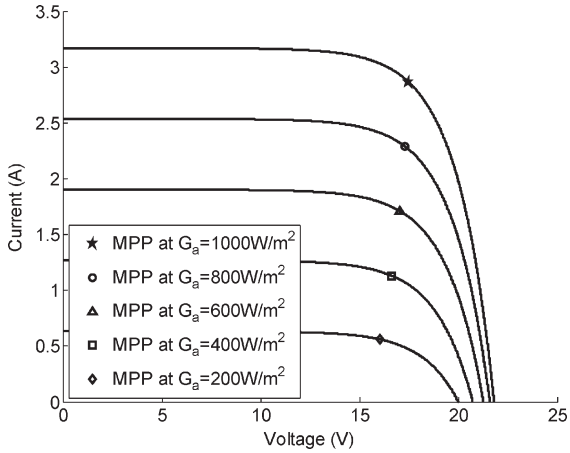

Fig. 1. Simulated I–V curves of BP350 influenced by insolation when the cell temperature is constant at 25 °C.

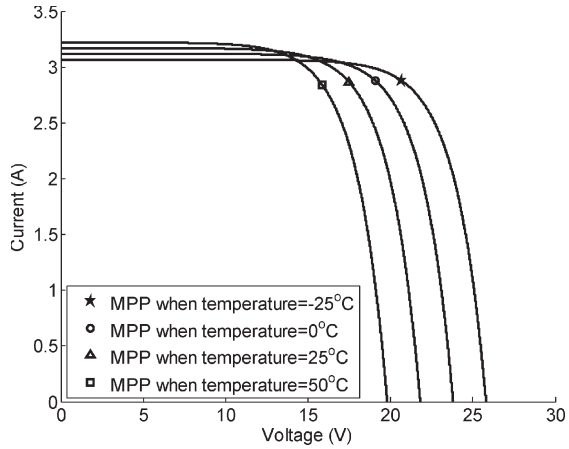

Fig. 2. Simulated I–V curves of BP350 influenced by cell temperature when the insolation is constant at 1000 W/m^2.

The ideal control variable that characterizes the MPP should be constant or should change slowly within a certain range. As a result, the photovoltaic voltage is preferable because of the advantages described here.

Fig. 1 illustrates that the changing radiation varies the photovoltaic current dramatically. The fast dynamics of insolation is usually caused by a cover of mixed rapid moving clouds. If the photovoltaic current is used as the set point, the MPP tracking requires fast dynamics to follow a wide operating range from 0 A to the short-circuit current, depending heavily on weather conditions. Nevertheless, the changing insolation slightly affects the voltage of MPP V_{MPP}, as shown in Fig. 1. Fig. 2 shows that the cell temperature is the major factor that shifts V_{MPP} significantly to follow the change. However, the

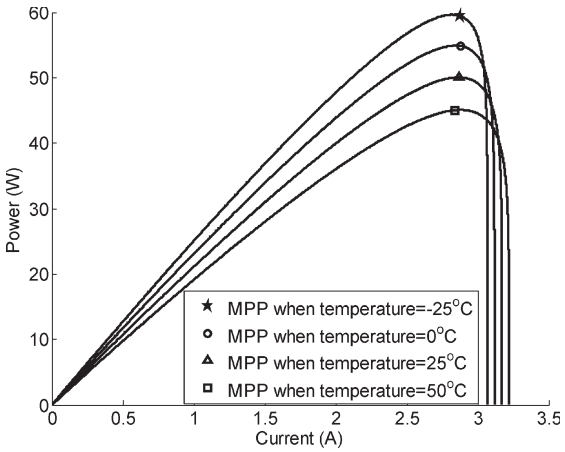

Fig. 3. Temperature effect on the relationship of power and current of the BP350 solar panel with a constant insolation equal to 1000 W/m^2.

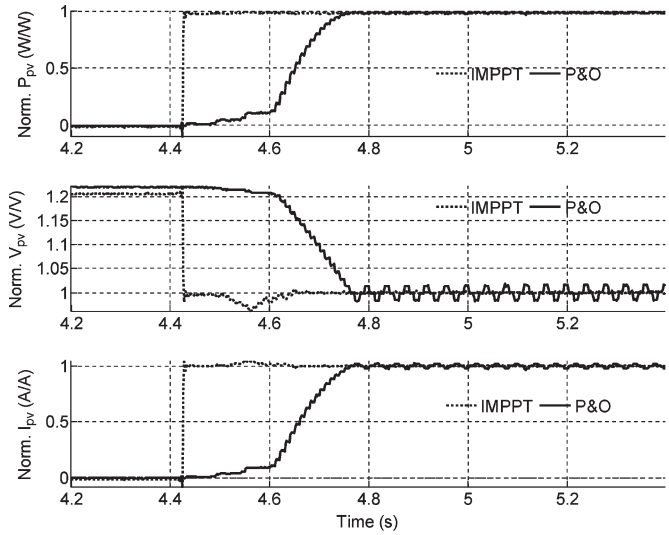

Fig. 4. Measured start of the MPP tracking between IMPPT and P&O.

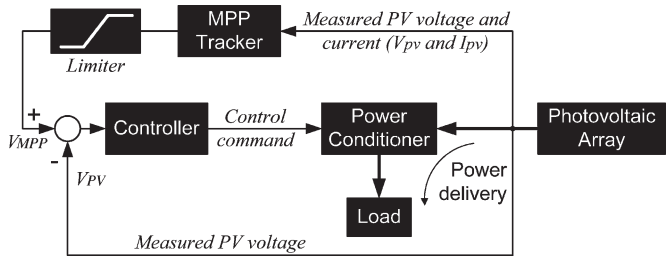

Fig. 5. Block diagram of the proposed control topologies.

cell temperature has slow dynamics and is always within a certain range.

Unlike the current of the MPP, the photovoltaic voltage of the MPP is usually bounded by 70%–82% of the open circuit voltage. This gives a lower bound and upper limit of the tracking range. When regulation of photovoltaic voltage is implemented, the MPP tracker can quickly decide the initial point according to the percentage of the open-circuit voltage. Fig. 4 shows a measured start of MPP tracking since the initial point of photovoltaic voltage is set to 80% of the open-circuit voltage, which is close to the true V_{MPP}. By comparison, the voltage regulation loop makes the starting time of MPP tracking much shorter than the operation of the perturbation and observation method (P&O), which is introduced in [1] and [2]. The moment of 4.43 s is the start point of the MPP tracking, as shown in Fig. 4. Before this moment, the photovoltaic modules are at the open-circuit condition. IMPPT represents the improved MPP tracking, in which the initial value of photovoltaic voltage is set to 80% of the open-circuit voltage. When the MPP is located, the IMPPT controller can stop continuous perturbations and keep only voltage regulation. By comparing to the P&O method, these result in a smoother steady state, as shown in Fig. 4.

This paper [3] shows that the photovoltaic current value at the MPP is close to about 86% of that of the short-circuit current. Because the photovoltaic current dramatically varies with insolation, the transient response of MPP tracking can occasionally cause the photovoltaic current to saturate at the short-circuit current. This should be prevented because its nonlinear feature causes a sudden voltage drop and results in both instability and power losses. However, for the regulation of photovoltaic voltage, voltage saturation can be easily avoided because a controller knows that its operating range is about 70%–82% of the open-circuit voltage. Furthermore, good-quality measurement of the voltage signal is cheaper and easier than that of current detection.

As a result, the recommended control structure is shown in Fig. 5. The controller regulates the photovoltaic voltage to follow a time-variant set point, which represents the voltage of MPP V_{MPP}. The value of V_{MPP} is continuously tracked and updated by the MPP tracker. Therefore, the regulation performance of the photovoltaic voltage is important for MPP tracking.

II. Modeling

It is necessary to regulate the photovoltaic voltage, as discussed in the last section. However, both photovoltaic modules and switching-mode converters demonstrate nonlinear and time-variant characteristics, which make a regulator design difficult. This paper will present a mathematical analysis of a specific photovoltaic system that includes a photovoltaic module and a boost dc–dc converter. The nonlinear system is characterized as several linear models within a certain range and time period. The linearization process is based on the fact that a model is linear in the incremental components of inputs and outputs around a chosen operating point (i.e., small-signal model). These models are suitable for the advanced controller design by using Youla parameterization, which is advantageous and introduced in [4].

A. Linear Approximation of Photovoltaic Characteristics

The characteristics of photovoltaic modules are nonlinear and time variant, as shown in Figs. 1–3. In electrical circuits, the resistance is defined as the ratio of the voltage across a circuit element to the current through it. However, the ratio of the voltage across a photovoltaic cell to the current through it varies with either the voltage or current. The ratio of the change

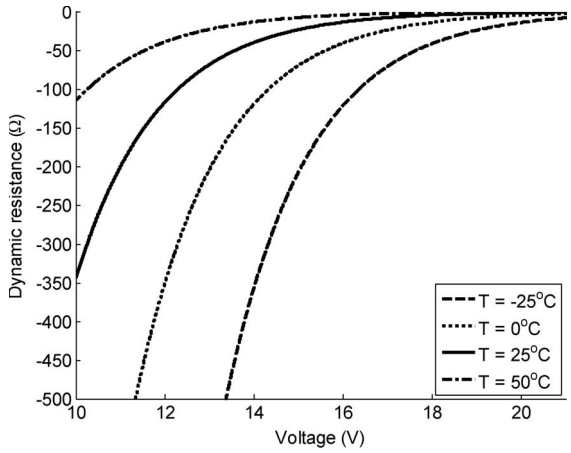

Fig. 6. Dynamic resistances versus photovoltaic voltage for four levels of cell temperature.

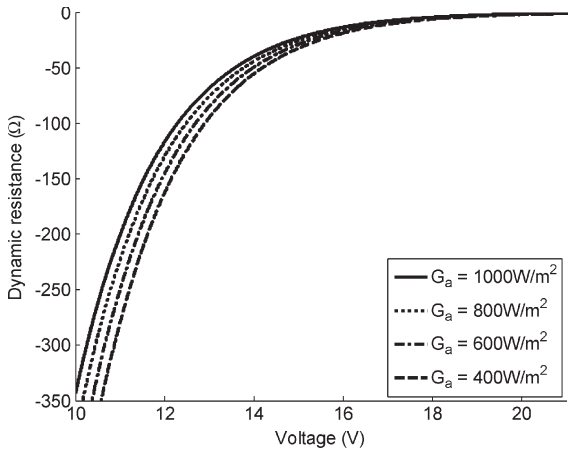

Fig. 7. Dynamic resistances versus photovoltaic voltage for four levels of insolation.

in voltage to the change in current is known as the dynamic resistance, which represents the slope of the resistance curve. The dynamic resistances of photovoltaic cells are negative although the static resistance of the circuit element is defined as positive.

Derived from the equivalent circuit shown in [5], the current through a photovoltaic cell can be represented by (1) and (2), where i represents the photovoltaic current, v symbolizes the photovoltaic voltage, v_t is the thermal voltage, R_S is the series resistor, $i_{\rm ph}$ is the photo current, and $i_{\rm sat}$ is the saturation current of the diode. Differentiating (1) leads to a dynamic resistance $r_{\rm pv}$ represented by (3) and (7), which is a function of the photovoltaic voltage. The cell temperature can vary the values of v_t, $g_{\rm pv}$, R_s, and $i_{\rm sat}$. The following analysis is based on a specific photovoltaic module BP350. Fig. 6 shows the plots of the dynamic resistance versus the photovoltaic voltage for various cell temperatures. Although the relationship of $r_{\rm pv}$ and insolation G_a is not shown in (7), there is some minor interaction, which can be referred to the product datasheet and can be shown as Fig. 7. Therefore, $r_{\rm pv}$ has the time-variant characteristics affected by both insolation and temperature. The dynamic resistance can be numerically approximated as (8), where $\hat{v}_{\rm pv}$ symbolizes a small increment of voltage and $\hat{i}_{\rm pv}$ stands for a small increment of electric current, i.e.,

$$i = i_{\rm ph} - i_{\rm sat}(g_{\rm pv} - 1) \tag{1}$$

$$g_{\rm pv} = e^{\frac{v+iR_s}{v_t}} \tag{2}$$

$$r_{\rm pv} = \frac{dv}{di}. \tag{3}$$

Under the steady-state conditions of irradiance and temperature, $i_{\rm ph}$ and $i_{\rm sat}$ are constant in (1). Differentiating (1) gives

$$1 = -i_{\rm sat}\frac{dg_{\rm pv}}{di}. \tag{4}$$

Substitution of (2) into (4) gives

$$1 = -i_{\rm sat}d\frac{\left(e^{\frac{v+iR_s}{v_t}}\right)}{di}. \tag{5}$$

From (5), we have

$$1 = -\frac{i_{\rm sat}}{v_t}e^{\frac{v+iR_s}{v_t}}\left(\frac{dv}{di} + R_s\right). \tag{6}$$

According to the definition of the dynamic resistance, (6) becomes

$$r_{\rm pv} = \frac{-v_t - i_{\rm sat}R_S g_{\rm pv}}{i_{\rm sat}g_{\rm pv}} \tag{7}$$

$$r_{\rm pv} \approx \frac{\hat{v}_{\rm pv}}{\hat{i}_{\rm pv}}. \tag{8}$$

To improve the MPP tracking, it is important to understand the distribution of dynamic resistances at the MPPs regarding different temperatures and insolation. Figs. 8 and 9 show the distribution variation influenced by different temperatures and insolations, respectively. The plots show that their amplitudes increase with decreasing cell temperature or with decreasing insolation. The largest amplitude happens when the insolation is at its lowest level and the cell temperature is at its lowest level. The range of $r_{\rm pv}$ is useful for a controller to estimate the present operating condition and to detect if the operating point deviates from the MPP.

To simplify the analysis, a piecewise linear approximation of the photovoltaic output characteristics is illustrated in Fig. 10. The I–V curve of the photovoltaic output is divided into four regions, namely: 1) the current-source region; 2) power region I; 3) power region II; and 4) the voltage-source region, according to the slope of the curve that is proportional to the dynamic resistance. The absolute value of dynamic resistance is small in the voltage-source region and big in the current-source region. The operating condition will eventually affect the system dynamics, which will be discussed in the succeeding sections. A normal operation generally starts from the voltage-source region and stays inside the power regions in steady state, so that the photovoltaic module can deliver the maximum available power.

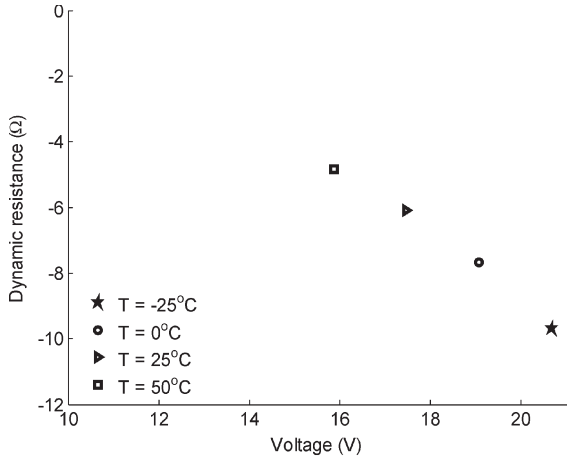

Fig. 8. Distribution of dynamic resistances influenced by cell temperature when the insolation is constant at 1000 W/m^2.

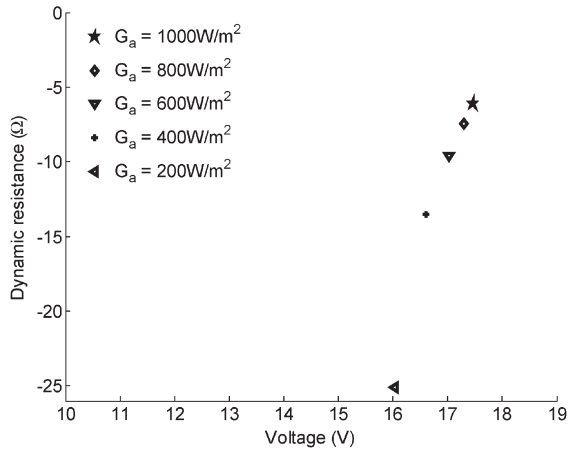

Fig. 9. Distribution of dynamic resistances influenced by insolation when the cell temperature is constant at 25 °C.

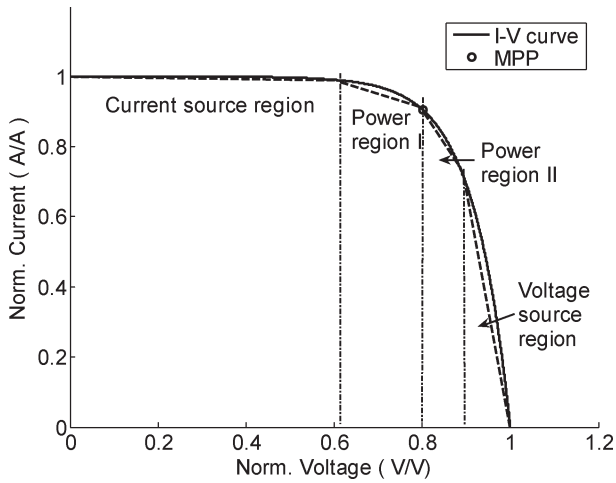

Fig. 10. Linear approximation of photovoltaic output characteristics.

B. Linearization of System Model

Nonisolated buck and boost dc–dc converters are widely used as photovoltaic interfaces due to their advantages of simplicity and efficiency. A buck dc–dc converter has a discontinuous input current and a continuous output current devoid of considering the input filter. On the contrary, a boost converter has a continuous input current and a discontinuous output current. These characteristics make their applications different when they are used as photovoltaic interfaces. The bench system in this paper adopts a boost topology, as shown in Fig. 11. The battery symbol in Fig. 11 implies a dc voltage bus, of which the voltage is relatively constant. Therefore, the system model can be obtained by the small-signal modeling method for pulsewidth-modulation (PWM) switched-mode power converters [6]. These averaged small-signal state-space models are derived and illustrated in (9) and (10), where $\hat{m}'$ represents the small decrement of duty ratio, $\hat{v}_{\rm pv}$ symbolizes the small increment of photovoltaic voltage, and $\hat{i}_{\rm pv}$ stands for the small increment of photovoltaic current. Other symbols in (9)–(14) refer to Fig. 11. The dynamic resistance is represented by $r_{\rm pvi}$ in (9) because it is a time-variant parameter, which depends on the operating condition. Derived from (9) and (10), the plant can be represented by the relationship between the small increment of photovoltaic voltage $\hat{v}_{\rm pv}$ and the small decrement of duty ratio $\hat{m}'$. This input–output transfer function in the S-domain $G_i(s)$ is illustrated in (11), where ω_i is the undamped natural frequency, K_0 is the gain, and ξ_i is its damping factor. Due to the time-varying characteristics, we are going to have four transfer functions according to the four regions defined in Fig. 10, i.e.,

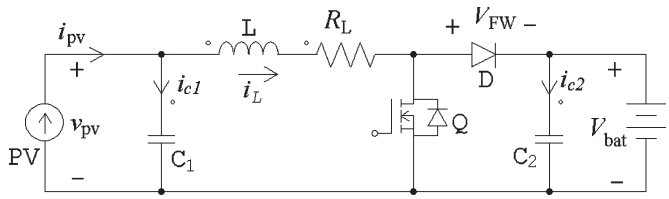

Fig. 11. Schematic diagram of the boost dc–dc converter.

$$\frac{d}{dt}\begin{bmatrix}\hat{i}_L\\ \hat{v}_{\rm pv}\end{bmatrix}=\begin{bmatrix}-\frac{R_L}{L} & \frac{1}{L}\\ -\frac{1}{C_1} & \frac{1}{r_{\rm pvi}C_1}\end{bmatrix}\begin{bmatrix}\hat{i}_L\\ \hat{v}_{\rm pv}\end{bmatrix}+\begin{bmatrix}-\frac{V_{\rm bat}-V_{\rm FW}}{L}\\ 0\end{bmatrix}\hat{m}' \tag{9}$$

$$\hat{y}=\begin{bmatrix}0 & 1\end{bmatrix}\begin{bmatrix}\hat{i}_L\\ \hat{v}_{\rm pv}\end{bmatrix} \tag{10}$$

$$G_i(s)=\frac{K_0}{s^2+2\xi_i\omega_i s+\omega_i^2}. \tag{11}$$

where

$$K_0=\frac{V_{\rm bat}+V_{\rm FW}}{LC_1} \tag{12}$$

$$\omega_i=\sqrt{\frac{-r_{\rm pvi}+R_L}{-r_{\rm pvi}LC_1}} \tag{13}$$

$$\xi_i=-\frac{-r_{\rm pvi}R_LC_1+L}{2r_{\rm pvi}LC_1\omega_i}. \tag{14}$$

C. Model Analysis and Experimental Verification

Based on the system parameters described in Table I, the magnitude and phase plots in Fig. 12 depict the frequency

TABLE I
SYSTEM PARAMETERS

Microcontroller	eZDSP™LF2407
Photovoltaic module	BP 350
Nominal input voltage	16V
Nominal output voltage	24V
Nominal solar power	50W
Switching frequency	40kHz
Inductance, L	260 μH
Input capacitor, C_1	22 μF
Series resistance of inductor, R_L	0.15Ω

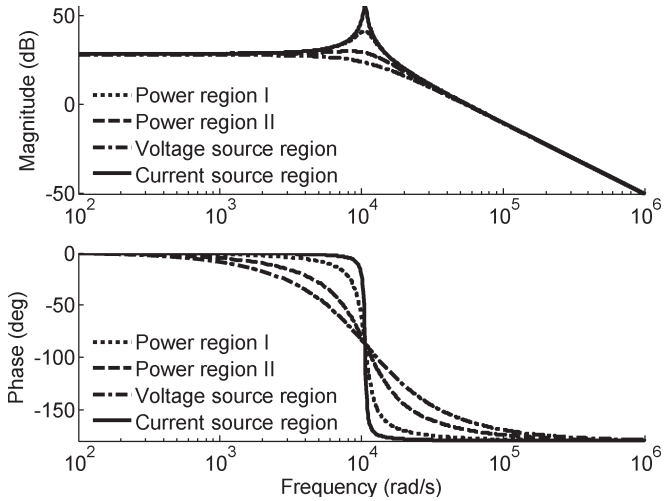

Fig. 12. Bode diagram of the photovoltaic system $G_i(s)$.

TABLE II
FREQUENCY PARAMETERS OF THE OPEN-LOOP MODEL

Operating point at	$r_{pvi}(\Omega)$	DC gain	ω_i (rad/s)	ξ_i
Current source zone	-350.00	26.52	10.60×10^3	0.0303
Power zone I	-15.71	26.28	10.64×10^3	0.1167
Power zone II	-3.20	25.34	10.84×10^3	0.4624
Voltage source zone	-1.67	24.34	11.06×10^3	0.8470

response of $G_{\rm pv}(s)$ for four different operating conditions, which are defined as the voltage region, current region, power region I, and power region II. The parameters of undamped natural frequency ω_i and damping factor ξ_i changes with the variation of operating points, as demonstrated in Table II. Listed in Table I, the value of R_L is 0.15 Ω.

From Table II, the different operating conditions slightly change the dc gain and undamped natural frequency ω_i. However, it significantly affects damping factor ξ_i. The system shows well-damped characteristics when the operating point is in the voltage-source region. When the operating point is close to the current-source zone, the damping factor reduces, while the dynamic resistance increases. When the operating point enters the current-source region, the plant becomes a lightly damped system, which is a difficult control problem, as described in [4].

The system is open-loop stable because there is no unstable pole. The normal operation of MPP tracking starts at the voltage-source region, which demonstrates a medium-damped feature. It is desirable that the operating point stays constantly within the power zones in steady state to achieve maximum

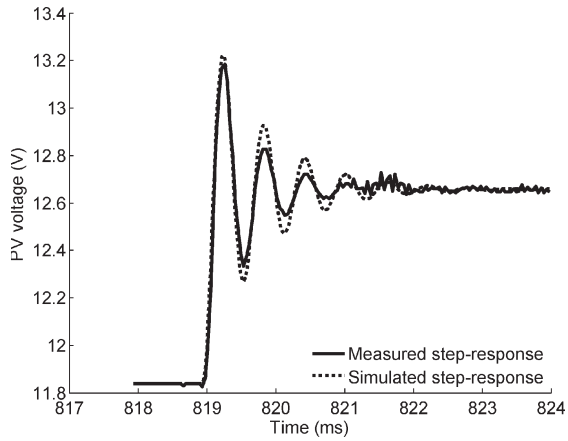

Fig. 13. Open-loop step-response of photovoltaic voltage in power region I.

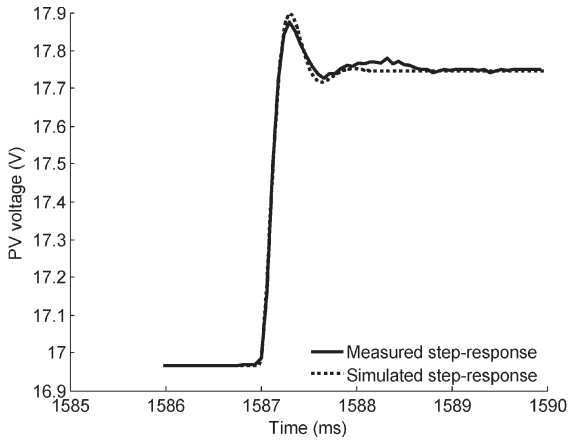

Fig. 14. Open-loop step-response of photovoltaic voltage in power region II.

power delivery from the photovoltaic cells. It turns out to be a lightly damped system when the operating point enters the current-source zone. This condition should be avoided since it results in reduced power output and some control issues of the lightly damped system.

A lower bound of the photovoltaic voltage is one way to prevent the operating point from deviating from the power zones. However, the cell temperature shifts the optimal operating voltage over a large range, as illustrated in Fig. 2. An alternative way is to use the lower bound of the dynamic resistance of the photovoltaic module. For example, if the lower limits of the operating condition of insolation and cell temperature are 200 $\rm W/m^2$ and -25 °C, respectively, the value of the dynamic resistance ranges from -40 to 0 Ω. When the detected dynamic resistance is lower than -40 Ω, the controller should increase the setting of the photovoltaic voltage to prevent the system from going into oscillatory state because the value of the dynamic resistance has changed the damping factor.

Based on the derivations of the linear models, computer simulations were performed to compare the behavior of the mathematical model to that of the physical device. The experimental tests illustrate the transient response in open-loop control with 5% step change of the duty cycle. The plots in Figs. 13 and 14 show the traces of the photovoltaic voltages regarding the measured values and those from the simulations

of the mathematical model. Measurement noise is unavoidable in most systems. In switching-mode converters, switching noise always appears in the ground plane and power supply. To avoid the measurement noise shown in the plots, the measured raw data are reprocessed through digital filtering. The digital filter is a second-order low-pass finite-impulse-response filter. This paper focuses on the power regions, which are the normal operating area. The dynamic response in Fig. 13 is different from that in Fig. 14 because they are based on two different operating conditions. As expected, in power zone I, the step response shows lightly damped characteristics, as shown in Fig. 13. In power zone II, it shows medium-damped feature, as shown in Fig. 14. This generally illustrates the effectiveness of linearization of the system model since the plots of the computer simulation are compatible with those obtained experimentally.

III. Closed-Loop Design

A successful closed-loop design needs to consider major control limitations. Three major issues will influence the control performance, namely: 1) the time-variant characteristics; 2) the lightly damped system; and 3) the time delay caused by digital control. First, the plant model changes with the variation of operating points and environmental condition. The control design should consider four regions and the worst case to ensure system stability. Second, the system shows lightly damped characteristics when the operating point accesses power region I or the current-source region. All control algorithms will be implemented in a digital controller that inevitably introduces the time delay caused by computation time and sampling rate. Experimental results and simulation will illustrate the effectiveness of the presented analysis, design, and implementation.

A. Youla Parameterization

Youla parameterization allows designers to choose the closed-loop parameters of undamped natural frequency $\omega_{\rm cl}$ and damping factor $\xi_{\rm cl}$. To ensure that proportional gain K_P is positive, a limit needs to be applied and to be expressed as (15), where ω_i stands for the plant undamped natural frequency and ξ_i is the plant damping factor. The damping ratio is selected as 0.7, and the undamped natural frequency is chosen to be 5.08 kHz to reshape the closed-loop performance, i.e.,

$$\xi_{\rm cl}\omega_{\rm cl} > \frac{\omega_i}{4\xi_i}. \tag{15}$$

B. Time Delays

The time lag introduced by the digital controller must be taken into account for the stability analysis. Time delays limit the achievable control bandwidth. To control the switching-mode converters, the new control variable is updated only at the beginning of the next switching period. The total delay can be considered to be equal to a switching period T_s. The delay time is 25 μs in this system because the switching frequency is 40 kHz. There are two ways to analyze the effect of time delay quantitively.

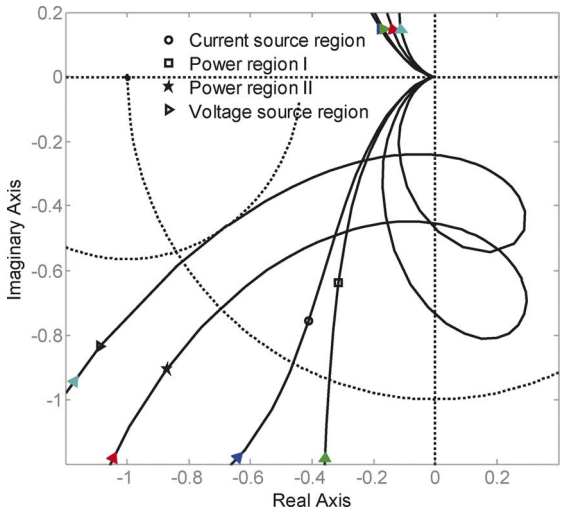

Fig. 15. Nyquist plots of the loop transfer functions $C(s)G_i(s)$ without considering time delay.

According to first-order Pade approximation [4], the time delay caused by the digital implementation can be expressed as

$$e^{-sT} \approx \frac{2 - sT_s}{2 + sT_s}. \tag{16}$$

The influence of time delay on a closed-loop system can also be explained as the reduced phase margin [7], which can be illustrated as (17). $\varphi_{\rm nmp}$ represents the nonminimal phase margin caused by the time delay. $\omega_{\rm CP}$ is the crossover frequency. The final phase margin at crossover frequency φ_m can be calculated as (18), where $\varphi_{\rm mp}$ is the phase margin of minimal phase part, i.e.,

$$\varphi_{\rm nmp} = -\omega_{\rm CP}T_s \tag{17}$$

$$\varphi_m = \pi + \varphi_{\rm mp} - \varphi_{\rm nmp}. \tag{18}$$

C. Controller Parameterization and Analysis

Based on the nominal converter model in the power region and following the procedure of Youla parameterization, the transfer function of the controller is determined as (19). $C(s)$ represents the controller transfer function in the S-domain, i.e.,

$$C(s) = \frac{s^2 + 2484s + 113\,300\,000}{2.92s^2 + 149\,200s}. \tag{19}$$

According to the study of past sections, there are large variations in the plant model since the damping ratio changes with the operating conditions from 0.03 to 0.85. The worst case is from the current-source region that shows lightly damped characteristics. Generally, the Nyquist diagram gives a graphical illustration of the system in terms of stability margins and maximum sensitivity. When the time lag is ignored, the plots in Fig. 15 demonstrate the Nyquist curves to represent the degree of stability. The definition of four

TABLE III
PARAMETERS OF STABILITY WITHOUT CONSIDERING THE TIME DELAY CAUSED BY DIGITAL CONTROL

Performance criteria	Current source region	Power region I	Power region II	Voltage source region
Phase margin	62.6°	69.9°	45.9°	34.8°
Cross freq (kHz)	3.01	2.97	1.39	1.20
Gain margin	∞	∞	∞	∞
Stability margin s_m	>0.57	>0.57	>0.57	0.57

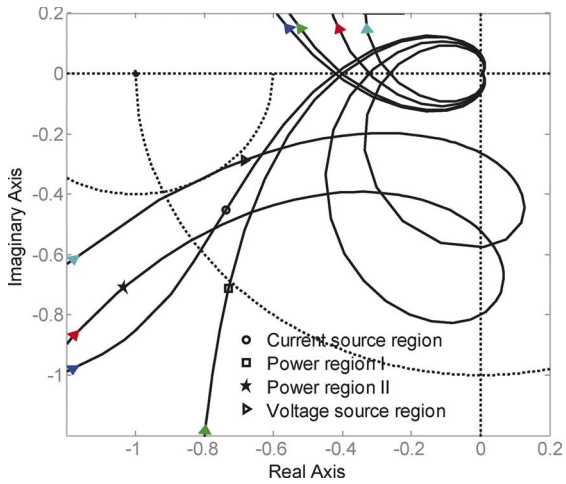

Fig. 16. Nyquist plots of the loop transfer functions $C(s)G_i(s)$ with considering time delay.

regions refers to Fig. 10. The plots also show the shortest distances between the Nyquist curve and the critical point $(-1+\mathrm{j}0)$, which can be interpreted as stability margin s_m. The parameters of stability and robustness are summarized in Table III.

The time lag introduced by the digital controller is the major component of nonminimum phase in this system. According to the approximation of the time delay as (16), the time delay can be added to the system transfer function, and the Nyquist curve can be replotted as Fig. 16. The parameters of stability and robustness are summarized in Table IV. By comparing Tables III and IV, the phase margin and stability margin are noticeably reduced by the time delay introduced by digital control. According to the rule of thumb in [4], the phase margins in Table IV are not significant enough to guarantee system robustness. As a result, further tuning is required for this specific system after Youla parameterization.

D. Controller Tuning

When the time lag of the digital controller is considered, the phase margin reduces to 24.1° in the worst case, which is not big enough for issues caused by modeling error and disturbance. Therefore, retuning is necessary to increase system stability and robustness.

Further tuning introduces tuning parameter γ_C, which can adjust the proportional gain. A reduced proportional gain can increase both the stability margin and phase margin. According to (19), the retuned controller is expressed as (20). The range of γ_C is shown in (21). The stability margin can be adjusted by changing the value of γ_C. For example, the Nyquist plots are shown in Fig. 17 when $\gamma_C = 0.2$. Thus, the parameters of stability and robustness are summarized in Table V. By comparing Tables IV and V, it is clear that system stability is improved, but the bandwidth is reduced by additional tuning after the Youla parameterization. After retuning, the controller transfer function becomes

$$C_\gamma(s) = \gamma_C C(s) \tag{20}$$

$$0 < \gamma_C \leq 1 \tag{21}$$

$$C_\gamma(s) = \frac{0.2s^2 + 497s + 22\,660\,000}{2.92s^2 + 149\,200s}. \tag{22}$$

E. Digital Redesign

The analog controller has been developed in the former section. By extending it to the digital control system, we need a digital redesign to obtain a digital controller by discretizing the analog controller. The sampling rate is chosen to be 40 kHz. In this section, two approximation methods, namely: 1) bilinear (Tustin) transformation and 2) matched pole-zero, are used and compared. According to the analog controller transfer function in (22), we have two digital controllers, i.e., (23) and (24) based on bilinear transformation and matched pole-zero, respectively. The comparison results of frequency responses between the discrete approximations and continuous-time controller are illustrated by Bode plots in Fig. 18. Both demonstrate satisfactory approximation inside the border of the Nyquist frequency, i.e.,

$$C_{\gamma\_\mathrm{Tustin}}(z) = \frac{0.04384 - 0.08212z^{-1} + 0.04124z^{-2}}{1 - 1.2205z^{-1} + 0.2205z^{-2}} \tag{23}$$

$$C_{\gamma\_\mathrm{Matched}}(z) = \frac{0.04052 - 0.07583z^{-1} + 0.03808z^{-2}}{1 - 1.2788z^{-1} + 0.2788z^{-2}}. \tag{24}$$

The controller is a 16-bit fixed-point digital signal processor (DSP). The constraints of digital implementation should be carefully handled to avoid the degradation of control performance. The major issues of the 16-bit fixed-point controller are from the quantization errors of the controller parameters and control variables because all data have to be truncated and stored as finite-length words. The clock of the DSP dramatically limits the resolution of duty cycle of the high-frequency switching converter. To design a switching-mode converter, there is always a tradeoff between the switching frequency, size of the system, and power losses in all components [8]. By considering the tradeoff, the switching frequency of the converter is 40 kHz in this system design. For such a low-power system, the

TABLE IV
PARAMETERS OF STABILITY WITH CONSIDERING THE TIME DELAY

Performance criteria	Current source region	Power region I	Power region II	Voltage source region
Phase margin	35.9°	43.5°	33.4°	24.1°
Gain cross freq (kHz)	6.04	6.26	7.15	7.97
Gain margin (dB)	2.49	3.07	3.76	11.5
Phase cross freq (kHz)	3.01	2.98	3.01	1.20
Stability margin s_m	>0.40	>0.40	>0.40	0.40

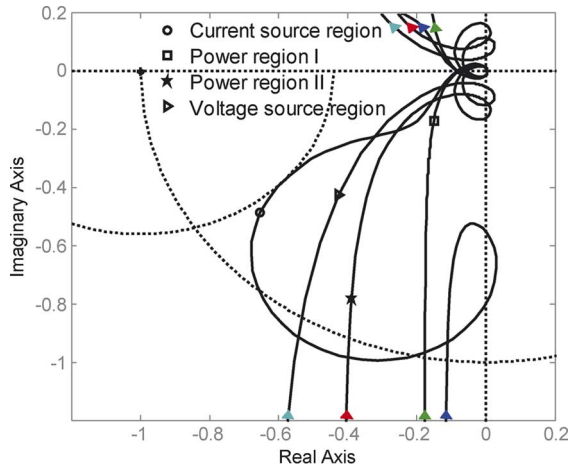

Fig. 17. Nyquist plots of the loop transfer functions $C_\gamma(s)G_i(s)$ after further tuning.

latest semiconductor technologies can make the switching much higher than 40 kHz without significant switching loss. However, according to the 40 MHz clock of the DSP used for this system, the resolution of duty cycle is only 0.1% when the switching frequency is 40 kHz. The DSP clock frequency generally limits the upper bound of the feasible switching frequency, when the DSP generates PWM signals directly.

F. Antiwindup

For PWM-type converters, the control variable is the duty cycle, which is in the range of 0%–100%. Saturation of the control variable is commonly caused by a step change of set point or load, which, in a controller implementation, results in integral windup. Therefore, an antiwindup control is essential for good closed-loop performance under these conditions.

The discrete controller can be represented by a difference equation, as shown in (25), which is transformed from (23). $\hat{m}'$ represents the small-signal control variable, and $e(k)$ is the error between the set point and the measured signal. Other parameters including a_1, a_2, b_0, b_1, and b_2 are derived from (23). The regulation flowchart is shown in Fig. 19, where $V_{\rm pv}$ represents the photovoltaic voltage, $V_{\rm ref}$ is the target voltage, $\hat{m}'_{\max}$ symbolizes the upper limit of the control variable, and $\hat{m}'_{\min}$ stands for the lower limit of the control variable, i.e.,

$$\hat{m}'(k) = -a_1\hat{m}'(k-1) - a_2\hat{m}'(k-2) + b_0e(k) + b_1e(k-1) + b_2e(k-2). \quad (25)$$

When the control variable reaches the limit, we can see that $\hat{m}'(k-1) = \hat{m}'(k-2)$ according to the flowchart shown in Fig. 19. Therefore, the controller difference equation (25) becomes (26). From the parameters in either (23) or (24), we know that $a_1 + a_2 = -1$. Hence, the controller difference equation is shown as (27) when saturation happens. The controller shown in (27) is a proportional controller in an incremental format. With the proposed controller structure, the integrator windup can be avoided because the recursive terms are automatically eliminated when the control variable reaches a limit, i.e.,

$$\hat{m}'(k) + a_1\hat{m}'(k-1) + a_2\hat{m}'(k-1) = b_0e(k) + b_1e(k-1) + b_2e(k-2) \quad (26)$$

$$\hat{m}'(k) - \hat{m}'(k-1) = b_0e(k) + b_1e(k-1) + b_2e(k-2). \quad (27)$$

IV. EVALUATION

The effectiveness of the proposed design is demonstrated by experimental evaluations with natural sunlight. Fig. 20 illustrates the regulation performance based on low solar radiation. Under this condition, the photovoltaic module can only output 7.6% of its rated power. The experiments intentionally applied periodical step-up and step-down changes in the voltage set points. They show stabilized regulations of photovoltaic voltage at three operating regions, namely: 1) the voltage-source region; 2) power region I; and 3) the current-source region. According to the analysis shown in Fig. 12 and Table II, the operating point significantly influences the damping factor. In the current-source region, the plant shows a lightly damped system, which is a difficult control problem, as described in [4]. With linear control techniques, there is always a tradeoff between system performance and robustness. To guarantee system stability in the four operating regions, the design sacrifices some performance by reducing the proportional gain of the system controller. According to the analysis in Table V and Fig. 17, the closed-loop design is optimized for power region I, which is one of the two major operating areas. As shown in Fig. 20(c), the closed-loop regulation illustrates smaller overshoots and undershoots in this region than in the voltage-source and current-source regions, as demonstrated in Fig. 20(b) and (d), respectively. To demonstrate the output characteristics during the test condition, the I–V curve was measured before each regulation evaluation, as shown in Fig. 20(a).

The major disturbance that has fast dynamics is the insolation variation, which is usually caused by the cover of mixed rapid moving clouds. To illustrate the effect of insolation disturbance, the simulated plots in Fig. 21 show the regulation performance against the disturbances caused by 100% step-up and step-down insolation changes, which are difficult to repeat in experimental

TABLE V
PARAMETERS OF STABILITY AFTER FURTHER TUNING

Performance criteria	Current source region	Power region I	Power region II	Voltage source region
Phase margin	49.0°	79.9°	66.7°	57.8°
Gain cross freq (kHz)	6.04	6.26	7.15	7.97
Gain margin (dB)	11.81	12.44	15.34	18.78
Phase cross freq (kHz)	1.71	0.63	0.58	0.51
Stability margin s_m	0.56	>0.56	>0.56	>0.56

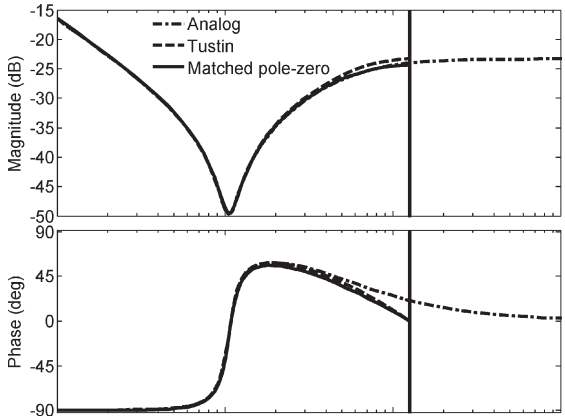

Fig. 18. Bode plots of the controller frequency response in the continuous and discrete domains.

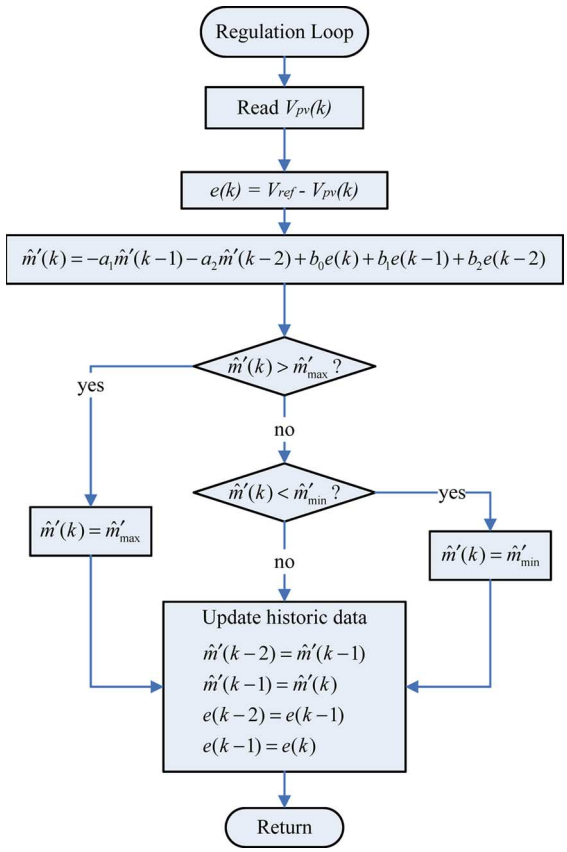

Fig. 19. Control loop for regulating the photovoltaic voltage.

tests with natural sunlight. $V_{\rm pv}$ is the photovoltaic voltage, $I_{\rm pv}$ symbolizes the photovoltaic current, and m is the control variable. The simulation shows the dynamic response against the disturbances caused by the step changes of insolation.

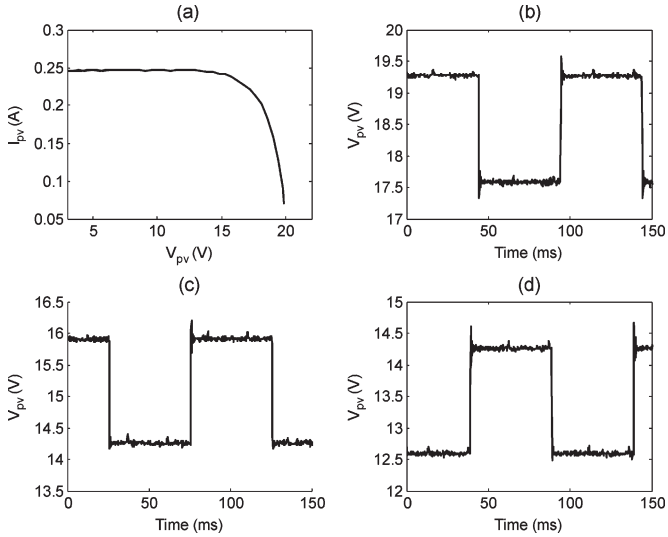

Fig. 20. Plots of photovoltaic-voltage regulation with low solar radiation. (a) Measured I–V curve. (b) Voltage-source region. (c) Power region I. (d) Current-source region.

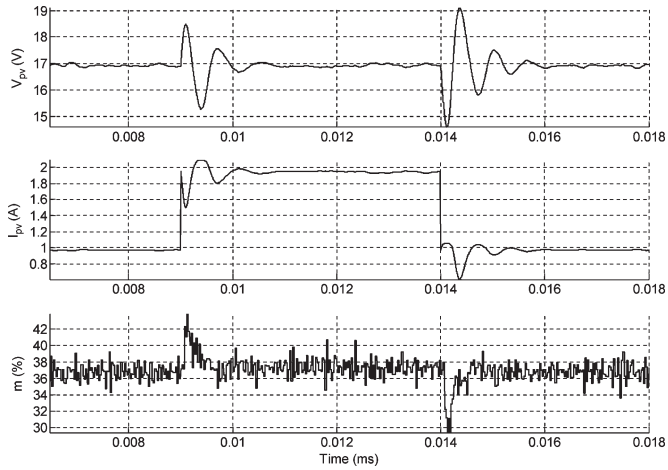

Fig. 21. Simulated results of regulation performance against the disturbance caused by 100% step change of the insolation level.

V. CONCLUSION

This paper has presented an in-depth analysis and modeling to discover the intrinsic characteristics of a photovoltaic power generation system. It also presented the use of Youla parameterization to design a control system for regulating the photovoltaic voltage.

In the bench system, both the photovoltaic modules and switching-mode converters present nonlinear and time-variant characteristics. It is important to approximate the nonlinear feature by a linear model since the techniques of linear control are

TABLE VI
SPECIFICATION OF PHOTOVOLTAIC MODULE BP350

Model	BP350
Photovoltaic Cells	Multicrystalline silicon
Cell number	72
Manufacturer	BP Solar
Voltage at MPP @ ST[§]	17.3V
Current at MPP @ STC[§]	2.89A
Short-circuit current (*Isc*) @ STC	3.20A
Open-circuit voltage (Voc) @ STC	21.8V

better established and simpler than the case of nonlinear control. To ease the analysis, the operating range was divided into four regions, namely: 1) the current-source region; 2) power region I; 3) power region II; and 4) the voltage-source region according to relative output characteristics. The method of successive linearization simplifies the nonlinear problem back to the linear case. The system also shows the time-variant characteristics because both the mathematical models and experimental results show that the frequency response is different from one region to another. The major variation lies in the damping factor caused by the variation of dynamic resistance. The change of insolation and temperature also affect the values of dynamic resistance.

Based on these characteristics, a controller is designed through Youla parameterization. However, the computational lag that is introduced by the digital control reduces the system phase margin significantly. Therefore, further tuning is also presented to guarantee system stability and robustness. Finally, experimental and simulation results demonstrate the effectiveness of the presented analysis, design, and implementation.

APPENDIX

The photovoltaic module of BP350 is a product of the BP solar company. The specification is listed in Table VI.

REFERENCES

[1] E. Koutroulis, K. Kalaitzakis, and N. C. Voulgaris, "Development of a microcontroller-based, photovoltaic maximum power point tracking control system," *IEEE Trans. Power Electron.*, vol. 16, no. 1, pp. 46–54, Jan. 2001.

[2] N. Femia, G. Petrone, G. Spagnuolo, and M. Vitelli, "Optimization of perturb and observe maximum power point tracking method," *IEEE Trans. Power Electron.*, vol. 20, no. 4, pp. 963–973, Jul. 2005.

[3] M. A. S. Masoum, H. Dehbonei, and E. F. Fuchs, "Theoretical and experimental analyses of photovoltaic systems with voltageand current-based maximum power-point tracking," *IEEE Trans. Energy Convers.*, vol. 17, no. 4, pp. 514–522, Dec. 2002.

[4] G. C. Goodwin, S. F. Graebe, and M. E. Salgado, *Control System Design*. Upper Saddle River, NJ: Prentice-Hall, 2001.

[5] W. Xiao, W. G. Dunford, and A. Capel, "A novel modeling method for photovoltaic cells," in *Proc. IEEE 35th Annu. Power Electron. Spec. Conf.*, Aachen, Germany, Jun. 2004, pp. 1950–1956.

[6] R. D. Middlebrook, "Small-signal modeling of pulse-width modulated switched-mode power converters," *Proc. IEEE*, vol. 76, no. 4, pp. 343–354, Apr. 1988.

[7] K. J. Åström, "Model uncertainty and robust control," in *Lecture Notes on Iterative Identification and Control Design*. Lund, Sweden: Lund Inst. of Technol., Jan. 2000, pp. 63–100.

[8] I. Zverev, "Switching frequency related trade off's in a hard switching CCM PFC boost convert," in *Proc. 18th Annu. IEEE Appl. Power Electron. Conf. and Expo.*, Miami, FL, 2003, vol. 2, pp. 671–676.

Weidong Xiao (S'03) received the M.A.Sc. degree in electrical engineering from the University of British Columbia, Vancouver, BC, Canada, in 2003. He is currently working toward the Ph.D. degree at the University of British Columbia.

His research interests include power electronics and applications of renewable energy sources.

William G. Dunford (S'78–M'81–SM'92) received the degree in engineering from Imperial College, London, U.K., and the Ph.D. degree from the University of Toronto, Toronto, ON, Canada.

He was part of a team that models satellite batteries at Alcatel, Toulouse, France. He is currently a member of the Clean Energy Centre, University of British Columbia, Vancouver, BC, Canada. He has worked on photovoltaic applications for a number of years. His research interests include distributed systems, with particular emphasis on efficiency, power quality, and automotive applications.

Dr. Dunford was the General Chair of the IEEE Power Electronics Specialists Conference in 1986 and 2001.

Patrick R. Palmer (M'87) received the B.Sc. and Ph.D. degrees in electrical engineering from the Imperial College of Science and Technology, University of London, London, U.K., in 1982 and 1985, respectively.

He joined the faculty of the Department of Engineering, University of Cambridge, Cambridge, U.K., in 1985. He is currently an Engineering Fellow at St. Catharine's College, University of Cambridge (elected 1987). Since 2004, he has been an Associate Professor in the Department of Electrical and Computer Engineering, University of British Columbia, Vancouver, BC, Canada. He has extensive publications in his areas of interest and is the inventor on two patents. His research is mainly concerned with the characterization and application of high-power semiconductor devices, computer analysis, simulation, and design of power devices and circuits, and he has further interests in fuel-cell hybrid vehicles.

Dr. Palmer is a Chartered Engineer in the U.K.

Antoine Capel received the Ph.D. degree from the University of Toulouse, Toulouse, France.

After teaching at the University of Toulouse and at the University of Pernambouc, Recife, Brazil, he joined the European Space Agency as a Power System Engineer. In 1983, he joined Alcatel Espace, Toulouse, where he first managed the Power Supply Laboratory and was the Head of the Power System Simulation Division. He is currently with the School of Engineering, Universitat Rovira i Virgili, Tarragona, Spain. He is the holder of five U.S. patents.